GSICS Global Space-based Inter-Calibration System

Quarterly

doi: 10.25923/j6c7-9r34
Vol. 17 No 3, 2023
Guest Editor: Peng Zhang (CMA)

Newsletter– Fall 2023 Issue

CMA • CNES • ESA • EUMETSAT • IMD • ISRO • JAA • JMA • KMA • NASA • NIST • NOAA • ROSCOSMOS . ROSHYDROMET • SITP • USGS • WMO

Special Issue on CMA

Articles

News in This Quarter

Announcements

GSICS Related Publications

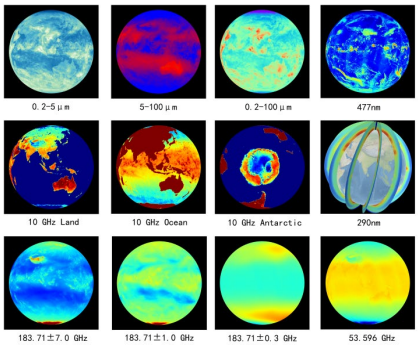

First images of FY-3F satellite

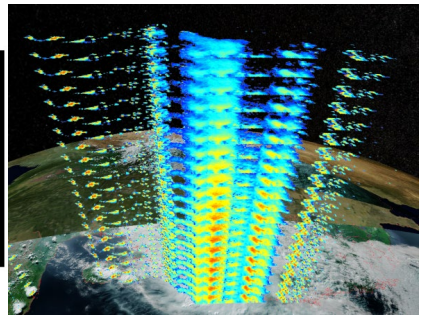

FY-3G precipitation radar image over southeastern China

Introduction on Chinese remote sensing satellites

By Chengli Qi, Ling Sun and Peng Zhang, (NSMC/CMA)

In the past few decades, China's space remote sensing technology has shown explosive development. Up to now, there are more than 60 civilian earth observation satellites in orbit, forming several Earth observation satellite series such as Fengyun, Haiyang, Ziyuan, Gaofen, Yaogan and Tianhui, which provide satellite remote sensing application services for meteorological and Marine monitoring and forecast, disaster prevention and reduction, resource exploration and mapping in China and around the world

China began to develop meteorological satellites in the 1970s, and as of November 2023, has launched 21 meteorological satellites, nine of which are in orbit. Fengyun-2 series are China's first generation of geostationary orbit meteorological satellites, a total of eight have been launched, currently in orbit are FY-2G and FY-2H, carrying two main payloads of scanning radiometer and space environment monitor. It can obtain daytime visible images, day and night infrared images and water vapor distribution maps and monitor solar activity and the space environment in the orbit of the satellite. FY-4 series are the second generation of China's geostationary meteorological satellites. FY-4A was launched in 2016, which equipped with Geostationary Interferometric Infrared Sounder (GIIRS) firstly in the geostationary orbit, as well as Advanced Geostationary Radiation Imager (AGRI), Lightning Mapping Imager (LMI) and Space Environment Monitoring Instrument Package (SEP). FY-4B launched in 2021, in addition to AGRI and GIIRS, it also carried a Geo High-speed Imager (GHI), and both of FY-4A and FY-4B are currently in operational status. Fengyun-3, the second generation of polar orbiting meteorological satellites in China, with a total of seven launched. The major launches in recent years include FY-3E early morning satellite launched in 2021, which realizes the first active radar wind field remote sensing detection among Fengyun-series

satellites, FY-3G inclined-orbit precipitation satellite launched in April of this year, which has the capability of microwave active and passive combined measurement of the three-dimensional structure of precipitation, as well as the FY-3F an AM orbit satellite launched in August of this year, two of hyperspectral instruments in the ultraviolet to visible spectrum were added, using the combination of nadir and Limb observation model to enhance the detection capability of atmospheric composition and pollution gases and aerosols. Fengyun-2, Fengyun-3 and Fengyun-4 complement with each other in terms of coverage and detection functions and have become important tools for China to obtain global data and meet the needs of regional catastrophic weather and environment monitoring, meteorological services and earth system scientific research. They have also been included in the global Earth Observation operational satellite series by the World Meteorological Organization of the United Nations, are playing an increasingly important role in international meteorological disaster prevention and reduction.

Since the 1980s, China began to develop a series of Ziyuan satellites, including a series of "Ziyuan-1" to "Ziyuan-3", providing key remote sensing data for land and resources survey, environmental monitoring, agriculture, forestry and water conservancy and other fields. The "Ziyuan-1" consists of six satellites, mainly equipped with spectral cameras, for the monitoring, guideline and management of land resources, forestry, water conservancy, environmental protection, and other fields. The "Ziyuan-2" satellite (ZY-2) is a transmission remote sensing satellite, which launched 01, 02 and 03 satellites from 2000 to 2004. Equipped with infrared and visible cameras, multi-spectral scanners, microwave radiometers, multi-functional radars and other remote sensing payloads, the series of satellites are used in many fields such as land and resources exploration, environmental monitoring and protection, urban planning, and crop yield estimation. Launched in 2012, Ziyuan-3 (ZY-3) is China's first civilian high-resolution optically transmitted stereoscopic mapping satellite. Equipped with a multi-spectral camera, it provides high-resolution stereo images of 2.1 meters and multi-spectral images of 6 meters, serving many fields such as land resources investigation and monitoring, disaster prevention and reduction, agriculture, forestry and water conservancy, and ecological environment.

China began to launch Marine satellites in 2002 and has launched eight of them so far, covering three series of ocean watercolor, ocean dynamic environment and ocean surveillance and monitoring. Ocean color series satellites are ocean remote sensing satellites with visible light and infrared imaging observation, mainly used for ocean color, water temperature and coastal zone observation. The Ocean-1 satellite family consists of four satellites, Ocean-1A, 1B, 1C and 1D. The Haiyang-1C and 1D satellites, launched in 2018 and 2020, constitute China's first Marine civil service satellite constellation, achieving dual-satellite and afternoon network observation. Five payloads are carried on board, ocean color and water temperature scanner, coastal zone imager, ultraviolet imager, on-board calibration spectrometer, and automatic ship identification system. It can realize long-term, continuous, and stable detection of global ocean watercolor, and provide monitoring support in sea ice, red tide, oil spill and other aspects. The series of Marine dynamic environment satellites, including the Haiyang 2A, 2B, 2C and 2D satellites and the China-France Marine Satellite, are mainly used to monitor a variety of Marine dynamic environmental parameters such as global all-weather sea surface wind field, wave height, sea surface height and sea surface temperature, and provide support services for Marine disaster prevention and reduction, Marine environmental protection, and Marine scientific research. Launched in 2018, the China-France Ocean Satellite is a joint scientific research and test satellite between China and France. It is mainly used for the monitoring of the Marine dynamic environment, and for the first time has achieved large-scale, high-precision synchronous observation of ocean surface winds and waves.

The Tianhui series satellites are China's stereoscopic mapping satellites, which have been under development since 2010 and are mainly used for scientific experimental tasks in the fields of scientific research, land and resources census, mapping, and other fields. Tianhui No. 01, 02, 03, 04 are mainly equipped with three categories of cameras. These include a three-line array camera,a 2-meter high resolution panchromatic camera and a multi-spectral camera. Tianhui-2 is a distributed interferometric microwave mapping satellite system, mainly equipped with interferometric synthetic aperture radar, which is used to generate global high-precision three-dimensional surface model and ground measurement elevation. Subsequently. Tianhui No.4, No.5 and No.6 surveying and mapping satellites were launched, mainly for tasks such as geographic information surveying and mapping, land and resources survey and scientific experimental research.

China began developing the Gaofen series of satellites from 2013. The Gaofen-1 and Gaofen-2 satellites are mainly equipped with high-resolution spectral cameras to provide high-definition image data. Based on radar technology, the Gaofen-3 satellite is

Return to Page One

doi: 10.25923/j6c7-9r34

equipped with a C-band multi-polarization synthetic aperture radar (SAR) satellite with a resolution of 1 meter, which can obtain stable and reliable high-resolution SAR images, playing an important role in disaster monitoring, emergency rescue and other fields. Gaofan-4 is a geostationary satellite, equipped with a gaze camera, visible, multi-spectral and infrared imaging capabilities, better to solve the problem of high time resolution. Gaofen-5, launched in 2018, is the only hyperspectral satellite in the Gaofen-series, with a spectral resolution of up to 0.5 nanometers. For the first time, the satellite carried a total of six payloads: atmospheric trace gas differential absorption spectrometer, atmospheric major greenhouse gas monitor, atmospheric multi-angle polarization detector, atmospheric environment infrared very high resolution detector, visible short-wave infrared hyperspectral camera, and full-spectrum spectral imager. It can monitor many environmental factors such as SO_2, NO_2, CO_2, CH_4, water quality etc. Gaofen-6 is a precise agriculture observation satellite, equipped with 2 meters panchromatic /8 meters multi-spectral high-resolution camera (width 90 km), 16 meters multi-spectral medium resolution wide camera (width 800 km), adding a "red edge" band that can effectively reflect the unique spectral characteristics of crops. Gaofen-7, launched in 2019, is a submeter-class high-resolution optical transmission stereoscopic mapping satellite that can map areas with complex terrain conditions.

This special GSICS Newsletter issue comprises six articles: the first, written by *Qiao Song et al.* propose a new post-hoc flat field measurement method for the solar X-Ray and Extreme Ultraviolet Imager onboard the Fengyun-3E Satellite which effectively removes instrumental non-uniformities from the original data. *Xingwei Hu et al.* present radiometric calibration assessing results of FY-4A/AGRI thermal infrared channels using CrIS and IASI. *Heyu Xu et al.* show a cross-calibration method for the Multi-Spectral Instrument (MSI) carried by Sentinel-2B using the hyperspectral remote sensor, the satellite calibration spectrometer (SCS) carried by Hai Yang (HY)-1C, as the reference sensor. In radiometric benchmark transferring domain, *Ning Wang et al.* introduce the methodology and results of an experiment designed to calibrate satellite optical payloads using reference payloads carried by high-altitude scientific balloons operating in stratosphere environments. FY-3G is a new satellite launched this year, *Honggang Yin et al.* present the preliminary calibration results of the Precipitation Measurement Radar onboard it. Finally, *Chao Liu et al.* develop an all-cloud target (ACT) calibration method for six MERSI-II reflective solar bands (RSBs) and correct the current MERSI-II reflectance biases to improve its calibration accuracy.

A New Post-hoc Flat Field Measurement Method for the Solar X-Ray and Extreme Ultraviolet Imager Onboard the FengYun-3E Satellite

By Qiao Song[1], Xianyong Bai[2], Bo Chen[3], Xiuqing Hu[1], Yajie Chen[4], Zhenyong Hou[4], Xiaofan Zhang[2], Lingping He[3], Kefei Song[3], Peng Zhang[1], Jing-Song Wang[1], Xiaoxin Zhang[1], Weiguo Zong[1], Jinping Dun[1], Hui Tian[4], and Yuanyong Deng[2]. [1]NSMC/CMA, [2]NAOC/CAS, [3]CIOMP/CAS, [4]PKU/SESS

Extreme ultraviolet (EUV) observations are widely used in solar activity research and space weather forecasting since they can observe both the solar eruptions and the source regions of the high-speed solar wind. Flat field processing is indispensable to remove the instrumental non-uniformity of a solar EUV imager in producing high-quality scientific data from original observed data. FengYun-3E (FY-3E) is a meteorological satellite operated in a Sun-synchronous orbit, and the routine EUV imaging data from the Solar X-ray and Extreme Ultraviolet Imager (X-EUVI) on board FY-3E has the characteristic of concentric rotation. Taking advantage of the concentric rotation, we propose a post-hoc flat field measurement method for its EUV 195 Å channel in an article [1].

We derived the flat field using the equations described in Section 2 of our article [1] and the result is presented in Figure 1. Figure 1(a) is the $[I(x, y, t) - I_d]_{\text{median}}$ image in the Cartesian coordinate system obtained by the median value of each pixel from a time series of 417 frames. After the processing, the small-scale components of the coronal radiation $I_s^h(x, y)$ are almost eliminated. From the image, we can see the residual large-scale coronal component $I_s^l(x, y)$, i.e., the quiet radiation with circular symmetry and the limb brightening pattern. We can also see the instrumental non-uniformity, i.e., the spot-like features and quasi-periodic grid-like features. Figure 1(b) is the median $I'(r)$ curve calculate Figure 1(a) to polar coordinates. Since solar active regions and other active features have been smoothed out, we can see the quiet coronal radiation from the solar disk.

Return to Page One

doi: 10.25923/j6c7-9r34

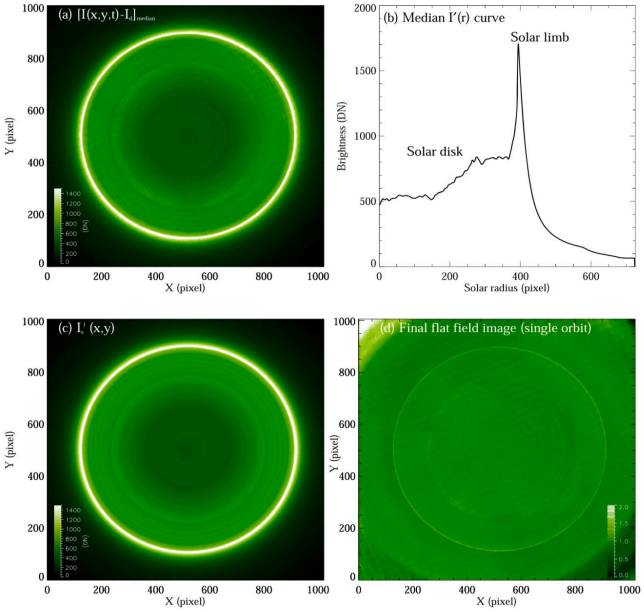

Figure 1. Calculation and generation process of the flat field image. (a) The dark corrected median data [I (x, y, t) - Id] median from time series images of the first orbit on 2021 October 29, and (b) features the median $I'(r)$ curve representing the quiet coronal radiation derived from (a). (c) The quiet coronal radiation I_S^I (x, y) image derived from (b), and (d) is the final flat field image of the time series data in Cartesian coordinates.

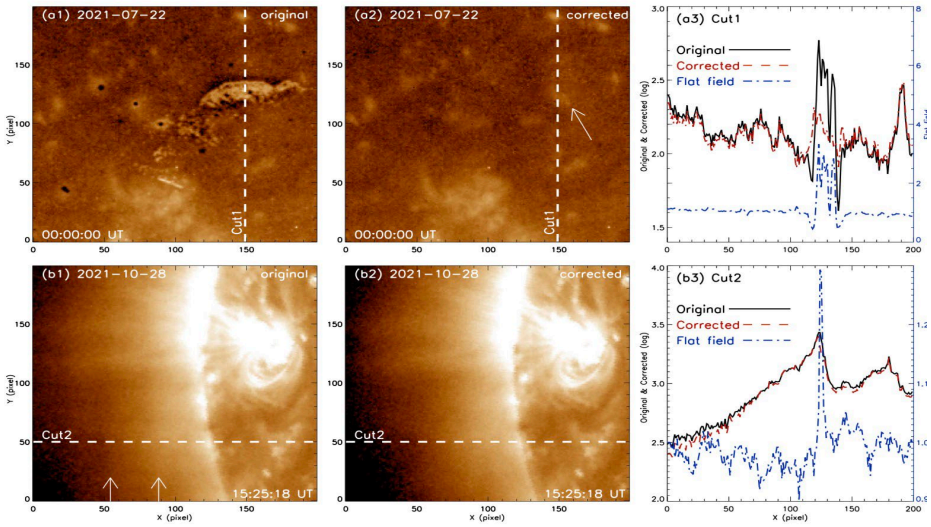

Figure 2. The local region before (left column) and after (middle column) the flat field processing. The solid, red dashed, and blue dot–dashed lines in the right column correspond to the original intensity, the intensity after flat field processing, and the values used in the flat field extracted from the dashed lines (i.e., Cut1 and Cut2) in the left and middle columns respectively. The arrow in (a2) indicates a coronal bright point that was revealed after the flat field processing. The two arrows in (b1) mark the positions of two quasi-periodic grid-like features.

and bright solar limb. Figure 1(c) displays the quiet coronal radiation I_S^I (x, y) image derived from Figure 1(b), and it can be seen that only bright limb and concentric circle features remain on this image. Figure 1(d) is the final flat field image, and there is mostly instrumental non-uniformity left, such as the grid-like features and some inhomogeneous intermediate-scale features. The flat field can be generated with cadences from hundreds of minutes (one orbit) to several days. Higher flat field accuracy can be achieved by employing more data.

With the flat field calculated from one day's data, we carried out the flat field processing of the original EUV 195 Å images for two days in July 2021 and October 2021, respectively. The results are arranged in Figures 2. Figures 2(a1) and (a2) are for a local region to better show the improvement after the correction of instrumental non-uniformity. On July 22, X-EUVI's self-cleaning mode was about to start, and there are multiple spot-like features on the image possibly caused by the adsorbed contaminant on the CCD detector. These spot-like features basically disappear after the flat field correction (Figure 2(a2)). The coronal bright point (see the arrow in Figure 2(a2) and the red dashed line in Figure 2(a3)), which is hardly found at the position of the spot-like feature, is clearly seen after the flat field correction. According to the flat field data, the contamination on the detector on 2021 July 22 is the most serious so far, and the successful correction of heavily contaminated images demonstrates the effectiveness of our method. In Figure 2(b1), we mark the positions of two grid-like features with arrows. Comparing the two images before and after flat field correction, the grid-like features almost disappear (Figure 2(b2)). A horizontal line in Figure 2(b1) is selected for a slice of Cut2. The original, flat field and flat field corrected values in the line are presented in Figure 2(b3). Due to the low amplitude of the grid-like features and the large dynamic range of coronal features, the visual effect of the flat field processing is not as significant as that for the spot-like features. However, the images show that the radial structures in the corona, such as coronal plumes and coronal streamers, are clearer after the flat field correction. Therefore, we believe that the flat field processing greatly improves the quality of the EUV images for the coronal radiation observation of X-EUVI. After dark and flat field corrections with our method, the comparative analysis results show that the X-EUVI 195Å coronal radiation is consistent with that from EUV images of the Atmospheric Imaging Assembly on board the Solar Dynamics Observatory. Figure 3(a1) is an X-EUVI 195 Å image at 09:11 UT on 2021

Return to Page One

doi: 10.25923/j6c7-9r34

October 28, and Figure 3(a2) is an almost simultaneous AIA 193 Å image for comparison. The coronal features of the X-EUVI image on both solar disk and solar limb agree well with those of the AIA image. We take horizontal and vertical slices on the images, where Cut3 is parallel to the solar Y-axis, and Cut4 is parallel to the solar X-axis. Figure 3(b1) depicts the brightness variation along Cut3, and features such as coronal bright points, active region loops, and a dark region corresponding to a coronal hole can be seen in this light curve. We normalized the brightness curve to facilitate comparative analysis, where the black line represents X-EUVI 195 Å images and the red dotted line corresponds to AIA 193Å data. The brightness variation along Cut4 shows a limb brightening pattern in the EUV wavelength (see Figure 3(b2)). Although the curves of the AIA 193 Å channel are sharper at the coronal loops, the bright points, solar limb, and other small-scale features, because of their higher spatial resolution, the overall trends of FY-3E/X-EUVI 195 Å and SDO/AIA 193 Å curves are consistent across the entire solar disk.

In conclusion, this method removes the small-scale and time-varying component of coronal activities by taking the median value for each pixel along the time axis of a concentric rotation data cube, and then derives the large-scale and invariable component of the quiet coronal radiation, and finally generates a flat field image. Results show that our method can measure the instrumental spot-like non-uniformity and the quasi-periodic grid-like non-uniformity. After flat field correction, these instrumental non-uniformities from the original data are effectively removed. Moreover, the X-EUVI 195 Å data after dark and flat field corrections are consistent with the SDO/AIA 193 Å images, verifying the suitability of the method. The post-hoc method does not occupy observation time, which is advantageous for space weather operations. Our method is not only suitable for FY-3E/X-EUVI but also a candidate method for the flat field measurement of future solar EUV telescopes.

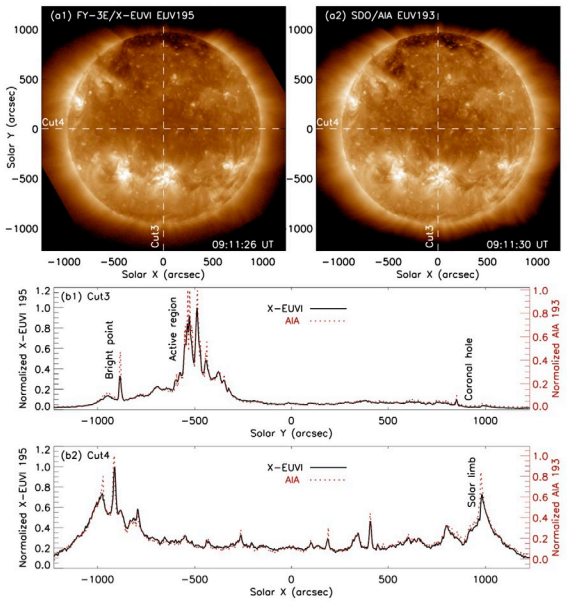

Figure 3. Comparison of X-EUVI 195 Å and SDO/AIA 193 Å images on 2021 October 28. Cut3 is parallel to the solar Y-axis, and Cut4 is parallel to the solar X-axis. In (b1) and (b2), the black line represents X-EUVI 195 Å and the red dotted line corresponds to AIA 193 Å light curves with normalized brightness.

Reference

[1] Q. Song et al., 2022, *Research in Astronomy and Astrophysics*, 22, 105001, DOI: 10.1088/1674-4527/ac7f0e

Assessing Radiometric Calibration of FY-4A/AGRI Thermal Infrared Channels Using CrIS and IASI

By Xingwei He, Na Xu, Xiaohu Feng, Xiuqing Hu Hanlie Xu, and Yi Peng, (NSMC/CMA)

The advanced geostationary radiation imager (AGRI) is one of the main instruments aboard the FY-4A satellite. The FY-4A AGRI TIR channels are assessed by comparing two well-calibrated hyperspectral radiometers, the cross-track infrared sounder (CrIS), and the infrared atmospheric sounding interferometer (IASI).

Fig. 1 shows the spectral response functions (SRF) of the 7 TIR channels of AGRI along with spectra showing the spectral coverage of CrIS\IASI. As neither CrIS nor IASI fully cover

Table 1. Data matching and screening constraints

Constraint	Criteria
Simultaneity	Observation time difference < 10 min
View geometry	Satellite sensor's view zenith angle < 30° $\lvert cos(\theta_{GEO})/cos(\theta_{LEO}) - 1\rvert < 0.01$
Collocation in space	Spatial distance < 2 km
Scene uniformity	SD_ENV < MaxSD; SD_FOV < MaxSD MaxSD = 8 count (Tb >= 250 K) MaxSD = 4 count (Tb < 250 K)

SRF of AGRI CH_08 (3.7 μm), and IASI exhibits significant instrument noise at cold temperatures, the calibration accuracy of CH_08 was not assessed in this study.

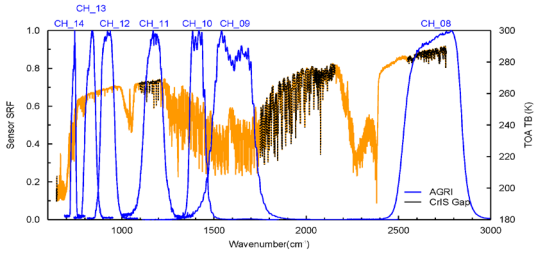

Fig. 1. SRFs of AGRI channels 8–14 from right to left (blue) overlain with CrIS/IASI spectral coverage, yellow line is the IASI Tb spectra, and the black part of the line shows spectral gap of CrIS.

Return to Page One

doi: 10.25923/j6c7-9r34

Systematic Error Type	Δx	Uncertainty(K) (Sensitivity,K/ Δx)		
		CH_09	CH_10	CH_11
Temporal Mismatch	60 s	- 0.018 (-0.0003)	0.002 (0.00004)	- 0.017 (-0.00028)
Longitudinal Mismatch	2.45 km	0.005 (0.0019)	0.005 (0.0020)	0.011 (0.0046)
Latitudinal Mismatch	2.45 km	0.006 (0.0023)	0.011 (0.0044)	0.035 (0.0141)
Geometric Mismatch	-0.0005	- 0.017 (34.5)	- 0.021 (41.7)	- 0.012 (24.8)
Temporal Mismatch	60 s	CH_12	CH_13	CH_14
Longitudinal Mismatch	2.45 km	- 0.016 (-0.00026)	- 0.014 (-0.00023)	- 0.003 (-0.00005)
Latitudinal Mismatch	2.45 km	0.015 (0.0060)	0.013 (0.0055)	0.004 (0.0017)
Geometric Mismatch	-0.0005	0.033 (0.0136)	0.032 (0.0131)	0.017 (0.0068)
Temporal Mismatch	60 s	- 0.008 (14.9)	- 0.009 (18.9)	- 0.036 (72.8)

Table 2: Summary of perturbations and corresponding uncertainty(sensitivities) for different systematic errors

Chanel	Sensor	slope	Intercept (K)	R	Num	Max(K)	Min(K)	mean(K)	SD(K)
CH_09	IASI	0.993	1.580	0.999	36982	5.742	-2.39	-0.27	0.29
	CrIS	0.994	1.321	0.999	75397	2.21	-1.94	-0.22	0.32
CH_10	IASI	0.994	2.039	0.999	30074	1.33	-2.41	0.52	0.23
	CrIS	0.994	2.093	0.999	62038	0.88	-2.13	0.51	0.25
CH_11	IASI	1.000	0.140	0.999	14176	2.78	-3.59	0.22	0.59
	CrIS	1.002	-0.500	0.998	31027	2.35	-3.38	0.15	0.62
CH_12	IASI	0.993	1.876	1.000	20556	3.42	-3.79	-0.18	0.41
	CrIS	0.994	1.651	1.000	42767	2.73	-3.05	-0.20	0.37
CH_13	IASI	0.993	0.073	0.999	22737	3.05	-3.13	-0.13	0.41
	CrIS	0.994	0.010	0.999	46304	2.93	-2.93	-0.16	0.39
CH_14	IASI	0.997	0.327	0.992	18506	3.02	-2.07	-0.53	0.58
	CrIS	0.989	2.455	0.991	38278	2.92	-2.30	-0.51	0.64

Table.3 Comparison of statistics of AGRI/TIR channel Tb vs. AGRI equivalent CrIS/IASI TB

1. GEO-LEO Collocations

Table 1 summarizes the constraint conditions for data matching and screening. After data matching and screening, the hyperspectral LEO CrIS\IASI radiances are convolved with the AGRI SRF to simulate the broad-channel GEO AGRI TIR channel radiance L, as follows:

$$L = \frac{\int_{\nu_1}^{\nu_2} R(\nu)S(\nu)d\nu}{\int_{\nu_1}^{\nu_2} S(\nu)d\nu} \quad ....(1)$$

2. Systematic Uncertainty Assessment

Table 2 summarizes the typical perturbations, Δx_j^s, caused by different types of systematic errors. The corresponding sensitivities, $\partial T/\partial x^s$, and the uncertainty of the six channels of AGRI are also shown.

3. GEO-LEO Tb bias

Table.3 summarizes the statistical parameters of the observed versus convolved AGRI Tb for six channels across the whole study period over the four-months from January 2020 to April 2020. The slope and intercept are unweighted linear regression coefficients between observed versus convolved AGRI Tb. The measured AGRI Tb values were in good agreement with the convolved CrIS/IASI Tb. All channels showed correlation coefficients (R) > 0.99 with a mean bias of less than 0.6 K.

Fig.2 (left) shows the Tb bias for the AGRI CH_13 measured Tb; it covers a wide Tb range from 200 K to 320 K. Fig.2 (right) shows the histograms of the collection number of the Tb bias. There are approximately twice as many CrIS collocations as IASI collocations because of their different scan patterns.

4. Diurnal Variations of Bias

Fig. 3 (bottom) shows the histogram of the collocation number at different hour bins, and the collocations number ranges from zero to tens of thousands. As shown in Fig. 3, during the ascension or descension of the LEO satellite, the collocation pairs with AGRI can last for nearly 6 hours, which enables us to evaluate the diurnal variation of AGRI bias at high temporal resolution Fig.3 (top) shows the diurnal variations in the mean Tb bias and SD

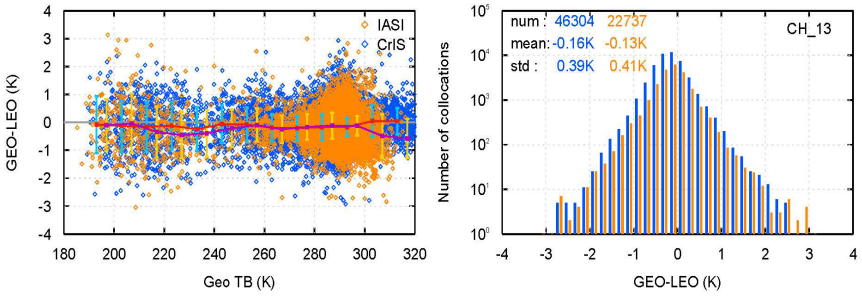

Fig. 2. (Left) scatterplots of the Tb bias vs. the AGRI Tb, the red and purple lines are the monthly mean Tb bias in 10K Tb bins between CrIS/IASI and AGRI with cyan and yellow error bars for SD respectively; and (right) histograms of the collection number of the Tb bias.

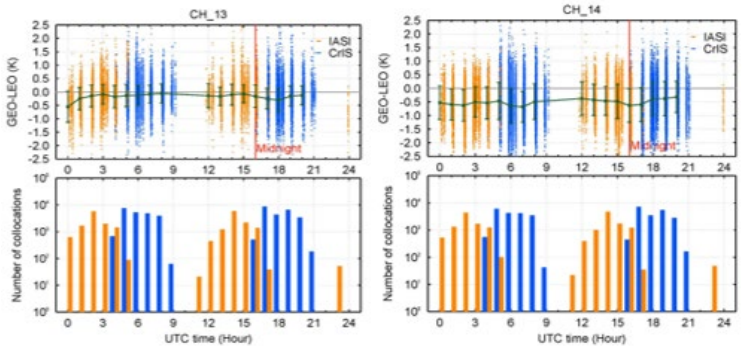

Fig. 3. (Upper) Tb bias diurnal variations collocated with IASI (in yellow) and CrIS (in blue) of two of the eight AGRI TIR channels over the four-month study period. The green segments show the hourly mean and SDs of Tb bias for each hourly bin. (Lower) accumulated hourly collocation pixels. The red vertical line is local midnight.

doi: 10.25923/j6c7-9r34

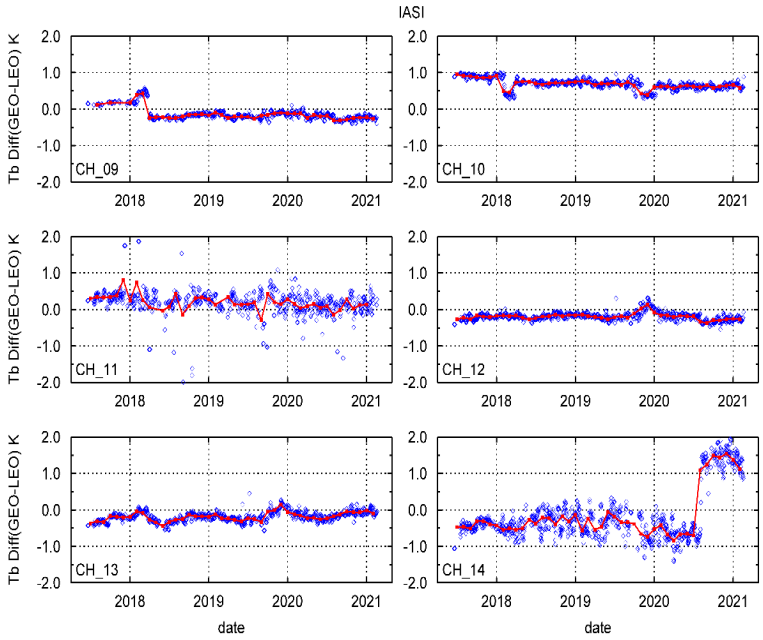

Fig. 4. Time series of the mean Tb bias of AGRI TIR channels with IASI, the blue dots are the daily collocations of Tb bias, and the red dots and lines are the monthly mean changes of Tb bias.

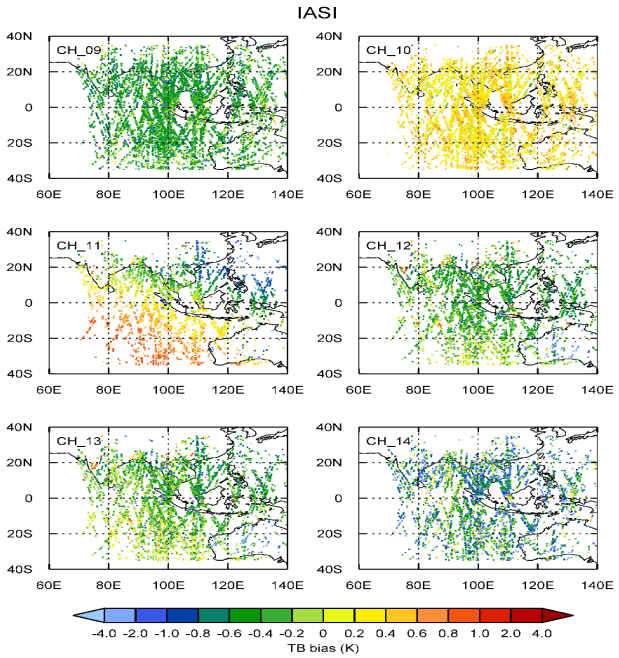

Fig. 5. Spatial distributions of Tb bias

5. Long-term Time Series of Bias

Fig.4 shows the long-term time series of bias with the monthly mean bias. There are bias jumps in February 2018, November 2019 and August 2020 for the operational calibration update. CH_10, CH_11 and CH_14 show gradual bias decreases; CH_12 and CH_13 exhibit seasonal variations. In general, Tb bias reach its maximum around June and minimum around February; CH_14 shows a gradual bias decrease with large fluctuation, the Tb bias jumps in late 2020 due to operational calibration update, this indicates that the calibration result is not satisfactory.

6. Spatial Distribution of Bias

For each TIR channel of AGRI, there are tens of thousands of collocations with IASI or CrIS. Fig.5 shows an example of the spatial distributions of Tb bias between the IASI-convolved AGRI and AGRI Tb of the collocations in January 2020. As FY-4A AGRI mainly scans over China and its neighboring ocean, the collocations were distributed within these regions. The Tb bias spatial distributions show different spatial patterns in the different channels.

CH_09 exhibits a cold Tb bias for the entire region and CH_10 shows a warm Tb bias. CH_14 shows the same pattern as that of CH_09, but with more variations. CH_12 and CH_13 is colder than those of IASI, and the bias values increase with latitude from south to north. The Tb bias appears to be correlated with the scene temperature, which has been discussed above, CH_11 exhibits obvious spatial distribution characteristics.

References:

[1] T. Hewison, X. Wu, F. Yu, and X. Hu, "GSICS Inter-Calibration of Infrared Channels of Geostationary Imagers Using Metop/IASI," *IEEE Trans Geosci Remote Sens,* vol. 51, no. 3, pp. 1160–1170, Mar. 2013.

[2] X. Wu, T. Hewison, and Y. Tahara, "GSICS GEO-LEO intercalibration: baseline algorithm and early results," *Proc. SPIE,* vol. 7456, pp. 745604-1–745604-12, Aug. 2009.

[3] F. Yu, X. Wu, M. K. R. V. Raja, Y. Li, L. Wang, and M. Goldberg, "Diurnal and Scan Angle Variations in the Calibration of GOES Imager Infrared Channels," *IEEE Trans Geosci Remote Sens,* vol. 51, no. 1, pp. 671–683, Jan. 2013.

[4] H. Xu, Y. Chen, and L. Wang, "Cross-Track Infrared Sounder Spectral Gap Filling Toward Improving Intercalibration Uncertainties," *IEEE Trans Geosci Remote Sens,* vol. 57, no. 1, pp. 509–519, Jan. 2019.

[5] T. J. Hewison, "An Evaluation of the Uncertainty of the GSICS SEVIRI-IASI Intercalibration Products," *IEEE Trans Geosci Remote Sens,* vol. 51, no. 3, pp. 1171–1181, Mar. 2013.

Return to Page One

doi: 10.25923/j6c7-9r34
GSICS Quarterly: Fall Issue 2023 Volume 17, No. 3, 2023

Radiometric cross-calibration of Sentinel-2B MSI with HY-1C SCS based on the near simultaneous imaging of common ground targets

By Heyu Xu[1], Wenxin Huang[1], Xiaolong Si[1], Qingjun Song[2,3], Xin Li[1], Xu Weiwei[1], Yue Ma[4], and Liming Zhang[1]

[1]Key Laboratory of Optical Calibration and Characterization, [2]National Satellite Ocean Application Service, [3] Key Laboratory of Space Ocean Remote Sensing and Application, [4]Beijing Institute of Space Mechanics & Electricity

Abstract:

To simplify the cross-calibration process and improve calibration frequency and accuracy, this paper proposes a cross-calibration method for the multispectral remote sensor Multi-Spectral Instrument (MSI) carried by Sentinel-2B using the hyperspectral remote sensor, that is, the satellite calibration spectrometer (SCS) carried by Hai Yang (HY)-1C, as the reference sensor and establishes the calibration process. Precise spectral response matching between SCS and MSI spectral bands is performed by the interpolation and iteration of hyperspectral data to eliminate the difference in band settings and significantly improve the accuracy of cross-calibration coefficients. The cross-calibration coefficients and offsets of MSIs B1~B7 and B8a were obtained by processing the earth observation images of the MSI and SCS on January 24, 2019. Then, the cross-calibration coefficients and offsets are applied to the ocean, farmland, and other ground objects with different reflectances, and the reliability and accuracy of the cross-calibration results are evaluated with the Moderate-resolution Imaging Spectroradiometer (MODIS) carried by Terra as a reference. To improve the accuracy of the evaluation, the spectral band adjustment factor between the corresponding channels of MSI and MODIS is used to correct the measured reflectance of MODIS based on the satellite calibration coefficient. The reflectance directly obtained by processing the MSI image is used as the MSI-measured reflectance, the reflectance obtained based on the cross-calibration coefficient is used as the MSI-calculated reflectance, and the reflectance corrected by the spectral band adjustment factor (SBAF) is used as the MODIS-calculated reflectance. The results show that the mean root-mean-square relative error (RMSRE) between the MODIS-calculated reflectance and the MSI-calculated reflectance is 2.16% and that the mean RMSRE between the MODIS-calculated reflectance and the MSI-measured reflectance is 3.05%, indicating that the reflectance corrected based on calibration coefficients is closer to the MODIS-calculated reflectance. Finally, each uncertainty source in the cross-calibration is analyzed, and the comprehensive uncertainty is found to be 4.03%, indicating that SCS can be used as a reference for MSI cross-calibration.

1. Introduction

The Hai Yang (HY)-1C satellite was successfully launched at the Taiyuan Satellite Launch Center on September 7, 2018. To solve the limitations associated with cross-calibration methods among multiple satellites and ensure a high onboard calibration accuracy of the satellite ocean color remote sensing instrument, for the first time, the SCS developed by the Beijing Institute of Space Mechanics and Electronics is carried onboard the HY-1C satellite platform and is used as the radiometric calibration reference source for cross-calibration of the Coastal Zone Imager (CZI), and other sensors perform cross-calibrations. As the cross-calibration reference, the SCS needs to be capable of high-precision spectral calibration and radiometric calibration tasks. Therefore, the Anhui Institute of Optics and Mechanics, Chinese Academy of Sciences, has designed an on-board "calibration diffuser + wavelength diffuser" calibration system for the SCS[1-4]. The research results show that SCS based on the onboard calibration system can achieve spectral calibration with a central wavelength error of 0.08 nm and a bandwidth error of 0.20 nm and can achieve absolute radiometric calibration with an uncertainty of better than 3%.

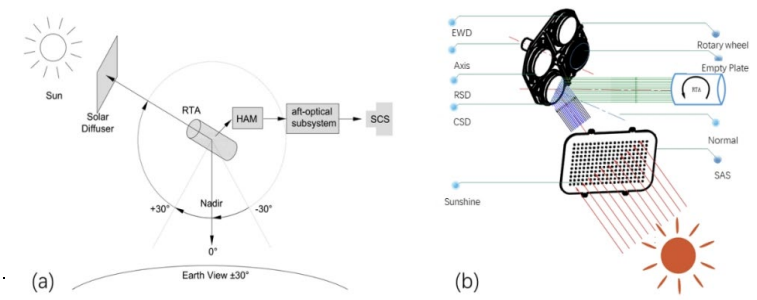

Fig. 1. SCS diagram: (a) SCS simplified block diagram; (b) schematic diagram of the SCS onboard calibration system.

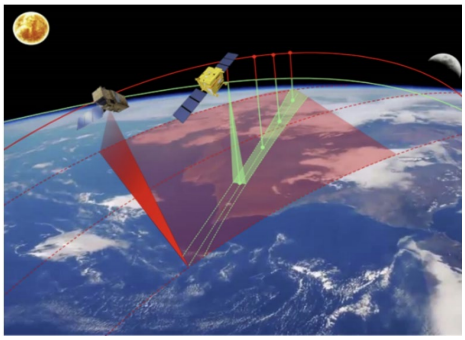

Fig. 2. Illustration of the cross-calibration method of MSI with SCS as the reference sensor.

doi: 10.25923/j6c7-9r34

MSI Band	B2	B3	B4	B6	Mean
RMSRE-1%	1.75	2.08	2.23	2.58	2.16
RMSRE-2%	3.53	2.43	3.11	3.17	3.06

Table 1.RMSRE results

Source of uncertainty	Uncertainty(K=2)
Uncertainty of SCS radiometric calibration	3.00%
Surface BRDF and atmospheric stability	2.00%
Radiation transmission path difference	1.50%
Spatial matching	1.00%
Comprehensive uncertainty	4.03%

Table 2. Cross-calibration uncertainty quantification results

This paper first introduces the cross-calibration process and method of the Sentinel-2B/MSI using the HY-1C/SCS as the reference sensor. The MSI calibration coefficients are obtained by processing the Earth-observation images taken by the MSI and SCS on January 24, 2019. Then, the MSI calibration coefficients are applied to different scenes, such as oceans, farmlands and soils, and the cross-calibration accuracy is validated by comparing the consistency of the results with MODIS-derived reflectance images.

Materials and methods

The optical path system of the SCS is equipped with a rotating telescope assembly (RTA) and half-angle mirror (HAM). When observing the Earth, light first enters the instrument through the RTA, then enters the fixed rear optical system through the HAM reflection, forms 101 continuous wavebands with a spectral resolution of 5 nm through the grating–splitting process, and finally reaches the load focal plane[5-6]. Through the combined rotation of the RTA and HAM, the SCS can switch between the Earth and diffuser observations. Figure 1(a) provides a simplified block diagram of the functional implementation of the SCS. The research team led by Professor Zhang Liming of Hefei Institute of Physical Science, Chinese Academy of Sciences, designed the onboard calibration system, as shown in Fig. 1(b).

In this paper, the SNO-x method is used for cross-calibration. It extends the SNO orbit to low latitudes so that cross-calibration can be carried out in a wide dynamic range[7-10]. Illustration of the cross-calibration between the MSI and SCS using the SNO-x method showing the field of view coverage area of the SCS as a reference (green strip) and MSI (red strip), as shown in Fig. 2.

Results and discussion

The coefficients and offsets of the MSI obtained by cross calibration, by analyzing and comparing the relative spectral response functions of the MODIS and MSI, bands B10, B4, B1 and B15 of MODIS are selected to validate B2~B4 and B6 of the MSI. The RMSRE results are listed in Table 1, where RMSRE-1 represents the RMSRE between the MODIS-calculated reflectance and the MSI-calculated reflectance and RMSRE-2 represents the RMSRE between the MODIS-calculated reflectance and the MSI-measured reflectance. RMSRE-1 is less than RMSRE-2, the mean RMSRE-1 value of each band is 2.16%, and the mean RMSRE-2 value of each band is 3.06%; that is, the MSI-calculated reflectance is closer to the MODIS-calculated reflectance, indicating that using the SCS as the reference sensor can achieve high-precision cross-calibration of the MSI.

Assuming that the error sources are mutually independent, according to the error propagation law, we can concur that the cross-calibration comprehensive uncertainty is the root mean square of the squared sum of all errors. The cross-calibration uncertainty values are listed in Table 2 below.

Conclusions

It can be seen from an analysis of the results that the mean RMSRE between the MODIS-calculated reflectance and the MSI-calculated reflectance is 2.16%, while the mean RMSRE between the MODIS-calculated reflectance and the MSI-measured reflectance is 3.05%. The MSI-calculated reflectance is closer to the MODIS-calibrated reflectance. The sources of uncertainty in cross-calibration are analyzed, and the results show that the comprehensive cross-calibration uncertainty is 4.03%, indicating that the cross-calibration results using SCS as the reference sensor have high accuracy and reliability, and SCS can be used as the reference sensor for the cross-calibration of other sensors.

Return to Page One

doi: 10.25923/j6c7-9r34

References

[1]. K. L. Zhang, Y. C. Zhang, and Y. Ma, "Design of on orbit cross calibration method for HY-1 C/D satellite," Spacecr. Eng. 28, 24–29 (2019).
[2]. H. Xu, L. Zhang, W. Huang, X. Li, X. Si, W. Xu, and Q. Song, "On-board absolute radiometric calibration and validation based on solar diffuser of HY-1C SCS," Acta Opt. Sin. 40(9), 0928002 (2020). 24.
[3]. H. Xu, 2020. Research on On-board Radiometric Calibration Method and Application of Space Hyperspectral Remote Sensor. University of Science and Technology of China, China.
[4]. MODIS on-orbit calibration and characterization," Proc. SPIE 8889, 88890U (2013). 10. H. Xu, W. Huang, X. Si, X. Li, W. Xu, L. Zhang, Q. Song, and H. Gao, "Onboard spectral calibration and validation of the satellite calibration spectrometer on HY-1C," Opt. Express 30(15), 27645–27661 (2022).
[5]. F. De Luccia, D. Moyer, E. Johnson, K. Rausch, N. Lei, K. Chiang, X. Xiong, J. Fulbright, E. Haas, and G. Iona, "Discovery and characterization of on-orbit degradation of the visible infrared imaging radiometer suite (VIIRS)rotating telescope assembly (RTA)," Proc. SPIE 8510, 85101A (2012).
[6]. X. Li, T. Yu, and C. Wang, "Design and implementation of a new half-angle mirror steering mechanism with high accuracy," Spacecr. Recovery Remote Sens. 40, 76–85 (2019).
[7]. Y. L. Shea, R. R. Baize, G. A. Fleming, D. Johnson, C. Lukashin, M. Mlynczak, K. Thome, and B. A. Wielicki. Climate Absolute Radiance and Refractivity Observatory (CLARREO) Pathfinder Mission: Status Overview. 2016.
[8]. S. Uprety, C. Cao, S. Blonski, and S. Xi, "Evaluating Radiometric Consistency between Suomi NPP VIIRS and NOAA-19 AVHRR using Extended Simultaneous Nadir Overpass in the Low Latitudes[C]," Conference on earth observing systems XVIII. 0.
[9]. C. Cao, M. Weinreb, and H. Xu, "Predicting Simultaneous Nadir Overpasses among Polar-Orbiting Meteorological Satellites for the Intersatellite Calibration of Radiometers[J]," J. Atmos. Oceanic Technol. 21(4), 537–542 (2004).
[10]. S. Uprety, C. Cao, X. Xiong, S. Blonski, and S. Xi, "Radiometric Intercomparison between Suomi-NPP VIIRS and Aqua MODIS Reflective Solar Bands Using Simultaneous Nadir Overpass in the Low Latitudes[J]," J. Atmos. Oceanic Technol. 30(12), 2720–2736 (2013).

High-altitude Balloon Payload for Satellite Radiometric Calibration and First Experiment Results

By Ning Wang, Lingling Ma, and Qiang Liu (Aerospace Information Research Institute, Chinese Academy of Sciences)

The on-orbit calibration and performance monitoring of satellite remote sensing payload calls for the support of the radiometric calibration source, which is of high stability, high reliability, and traceability. High-altitude scientific balloons have evolved into excellent platforms for conducting near-space scientific observations and experiments(Doi et al, 2019). In its CLARREO Pathfinder mission, NASA developed the HyperSpectral Imager for Climate Science (HySICS) as a prototype payload for space radiation benchmarking. In 2013 and 2014, two high-altitude scientific balloon flights carrying HySICS were conducted, providing scientific data for the validation of radiation benchmarking principles and the justification of the CLARREO mission (Kopp et al., 2017). Facing the problem of improving the accuracy of on-orbit radiometric calibration, a new strategy has emerged. First, radiometric benchmarks are transferred from laboratory to high-altitude balloon latforms. Then, by employing the simultaneous nadir overpass observations obtained from both the balloon platform payload and satellite observation, benchmark can be again transferred from space-borne platforms to satellites. This strategy has emerged as a viable approach to augment the accuracy of on-orbit radiation calibration.

Fig.1 Flight experiment and the track of the balloon payload's flight campaign

Return to Page One

doi: 10.25923/j6c7-9r34

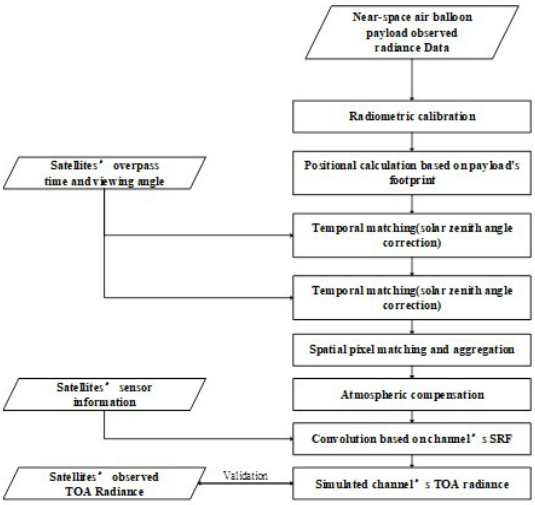

Fig.2 The flowchart for the data processing

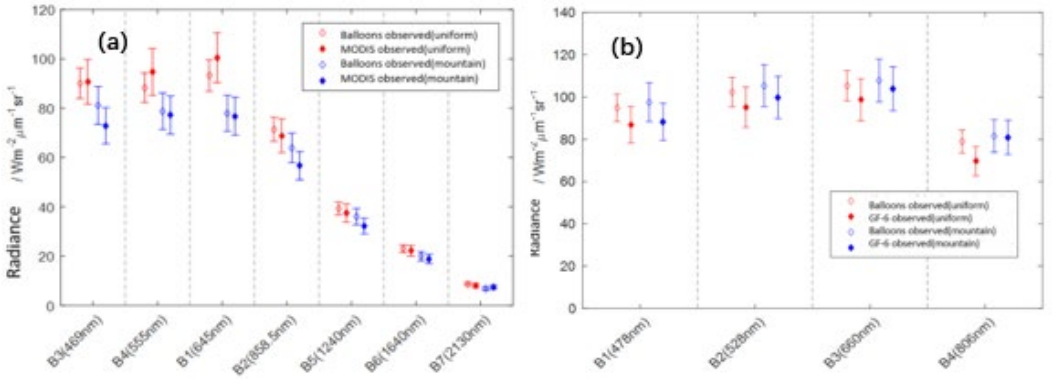

Fig.3 Results comparison and uncertainty analysis (a) Comparison between balloon payload and MODIS (b) Comparison between balloon payload and GF-6/WFI

Observations by high-altitude scientific balloons at stratosphere offer significant advantages of being closely parallel those of satellites, extended regional overpass periods and recyclability. These attributes render them suitable for transferring space radiometric benchmarks. This paper introduces the methodology and results of an experiment designed to calibrate satellite optical payloads using reference payloads carried by high-altitude scientific balloons operating in stratosphere environments.

Description of Stratosphere Radiometric Calibration System:

The stratosphere altitude radiometric calibration system is comprised of two primary subsystems: a high-altitude scientific balloon platform subsystem and payload subsystem. The former encompasses the balloon sphere, energy, flight control, and telemetry control subsystems. Specifically, the balloon sphere subsystem is responsible for providing lift and maintaining hover capabilities for the high-altitude scientific balloon, in addition to serving as a mounting platform for the effective payload. The energy subsystem supplies power to both the platform and the payload, whereas the flight control subsystem manages flight operations. The telemetry control subsystem is tasked with tracking and locating the balloon platform, facilitating remote measurement and control of flight parameters and operational status of equipment, and overseeing the collection and transmission of flight data. The payload subsystem is equipped with a visible-shortwave infrared hyperspectral radiometer as the reference payload. This payload is consisting of 1024 channels from 0.4μm to 2.4μm with a field-of-view of 3°. Its primary function is to conduct Earth observation within stratosphere altitude environments and to collect surface radiation data. An integrated high-altitude position and attitude measurement system is affixed to the radiometer to record the payload's position and orientation during observations, which is crucial for accurate geospatial positioning of the imaging data. Prior to deployment in the experiment, the instrument underwent rigorous laboratory spectral and radiometric calibration.

The spectral radiance reference radiometer developed for this purpose demonstrated a measurement uncertainty of less than 1.42%, as per the conducted assessments.

	Flat Area		Mountainous Area	
Uncertainty Factors	**Uncertainty Budget**	**Contribution / %**	**Uncertainty Budget**	**Contribution / %**
Radiometer Observation	0.83% ~ 1.42%	0.83 ~ 1.42	0.83% ~ 1.42%	0.83 ~ 1.42
Radiometer's Positional Accuracy	7.6%	1	7.6%	1.5
Spatial Uncertainty	10°	2	10°	3
Temporal Uncertainty	3h	2	15 min	0.5
Atmospheric Uncertainty	--	--	--	--
Field Uniformity Uncertainty	0.8~1.5%	0.5~1	6~10%	3~5
Combined Uncertainty		3.15 ~ 3.35		4.60 ~ 4.75

Table 1: The uncertainty budget of the flat area and mountainous area calibration

Return to Page One

doi: 10.25923/j6c7-9r34

Stratosphere Altitude Radiation Calibration Experiment

Introduction

To execute a stratosphere radiometric calibration experiment for satellite's optical payloads, specific meteorological and site conditions are essential for the deployment of high-altitude balloons. The chosen launch site for this experiment was positioned at coordinates 37°43'54.19"N, 95°20'22.57"E. On September 20, 2021, the said calibration experiment was conducted under clear sky condition using high-altitude balloons floating in stratosphere height, specifically in Da-Qaidam, Qinghai Province, China. The trajectory of the balloon flight is depicted in Figure 1, with a red box delineating the uniform region covered by the balloon. The data acquired from this experiment were subsequently compared with observations from the Terra/MODIS and China's GF-6/WFI. Notably, the MODIS satellite overpassed the area at 13:00 Beijing time, while the GF-6/WFI overpass occurred at 12:52 Beijing time on the same day. During its flight, the balloon traversed a homogenous sandy terrain from 10:15 to 10:45 and a mountainous region from 13:00 to 13:15.

Data Processing and Result Analysis

After obtaining the data from the stratosphere altitude balloons-borne radiometer, a series of data processing steps are undertaken. Initially, radiometric correction is applied to the observed data, followed by the computation of the geometric footprint, utilizing the payload's attitude information. Radiance data from the balloon payload observations is obtained by this process, enhanced by geometrical accuracy. The next phase involves the temporal and spatial matching of the data, which is then subject to atmospheric compensation. This step is complemented by the convolution of the balloon payload observed radiance data with the spectral response functions of the satellite channels, thereby calculating the observed radiance across these channels. Finally, the balloon payload simulated satellite dataset is then validated by comparing with the satellites' actual observed TOA radiance. The flowchart for this data processing procedure is illustrated in Figure 2.

Employing the aforementioned methodology, comparative analyses were conducted for the Terra/MODIS and GF-6/WFI observations. For uniform terrain scenes, it was observed that the relative difference between the radiance observed by MODIS and the simulated radiance for the stratosphere altitude balloons-borne payload is below 10% across all spectral bands, exhibiting an average absolute relative difference of 4.98%. Conversely, in mountainous terrains, despite the presence of notable temporal and spatial alignment between the balloon-based and satellite-based observations, a marked increase in this discrepancy was noted. Similar observations were made for the GF-6/WFI data, wherein the variance in most bands also did not exceed the 10% threshold. Both comparisons were detailed in Figure 3.

Uncertainty Analysis

Based on the observed data of the stratosphere altitude balloons-borne payload and the comparative analysis conducted, uncertainty estimates were formulated for both homogeneous (uniform) and heterogeneous (mountainous) landscapes. Given the radiometer's stable operational state during the flight experiment is like that of the laboratory calibration environment, its measurement uncertainty was determined to range between 0.83% and 1.42%, a finding corroborated by laboratory calibration results. The homogeneity of each terrain type was assessed using high-resolution images from GF-6/WFI. In uniform areas, this uniformity was estimated to fall between 0.8% and 1.6%, whereas in mountainous regions, it ranged from 6% to 10%.

The positional accuracy of the balloon's footprint during the flight was approximately 90 meters, resulting in an estimated error margin of about 7.6% within the defined footprint area. Further analysis of the GF-6/WFI imagery revealed that the uncertainty in radiance calculations attributed to spatial location mismatches was approximately 1% in uniform areas and 1.5% in mountainous regions. Uncertainty resulted from a 10° difference in observation viewing zenith angle, introduced uncertainties of 2% in uniform terrains and 3% in mountainous ones. Temporal uncertainties were also considered; a 3-hour time difference in uniform areas resulted in a 2% uncertainty when using MODTRAN simulations for solar irradiance corrections. In mountainous terrains, a shorter time difference of 15 minutes, coupled with variations in the solar zenith angle (approximately 0.5°), contributed to an uncertainty of less than 0.5%. Consequently, the overall calibration uncertainty for uniform and mountainous regions is estimated to be in the range of 3.15% to 3.35% and 4.60% to 4.75%, respectively, as detailed in Table 1.

Conclusion

Utilizing high-altitude scientific balloons as platforms in stratosphere environments for carrying optical radiometric payloads and using the payload as reference for satellite radiometric calibration offers significant advantages. This approach situates the payloads in an environment that encompasses most air masses and

Return to Page One

meteorological phenomena, thus closely mirroring the conditions of satellite observations in terms of radiation transmission. Such a setup notably diminishes the influence of atmospheric conditions on the simulation of radiation transmission. This paper presents the development and deployment of a stratosphere radiometric calibration system, outlines the methodology and execution of the flight experiments, and employs actual flight data for method validation. Additionally, it offers a preliminary analysis of uncertainties associated with the process. The combined uncertainty in radiance observation for uniform and mountainous terrains is estimated to range from 3.15% to 3.35% and 4.60% to 4.75%, respectively. The primary validation of this uncertainty analysis is corroborated by concurrent observations from MODIS and GF-6/WFI. However, the application of high-altitude scientific balloons in such research is still in a nascent phase, presenting numerous challenges in transporting radiometric reference payloads on stratosphere altitude platforms and in achieving radiometric chain transferring. A critical issue identified is the reliance solely on the stability of the radiometer's detector temperature control, presupposing alignment with laboratory measurement conditions. This approach, which extrapolates laboratory source uncertainty to characterize observational uncertainty in stratosphere altitude experiments, reveals a potential discrepancy in the uncertainty traceability chain. Consequently, there is a clear need for further research aimed at ensuring high-precision traceability to the International System of Units (SI) within stratosphere platforms.

Reference

Doi A, Kono Y, Kimura K, Nakahara S, Oyama T, Okada N, Satou Y, Yamashita K, Matsumoto N, Baba M, Yasuda D, Suzuki S, Hasegawa Y, Honma M, Tanaka H, Ishimura K, Murata Y, Shimomukai R, Tachi T, Saito K, Watanabe N, Bando N, Kameya O, Yonekura Y, Sekido M, Inoue Y, Sakamoto H, Kogiso N, Shoji Y, Ogawa H, Fujisawa K, Narita M, Shibai H, Fuke H, Ueharai K and Koyama S. 2019. A balloon-borne very long baseline interferometry experiment in the stratosphere: Systems design and developments. Advances in Space Research, 63: 779-793. [DOI: 10.1016/j.asr.2018.09.020]

Kopp G, Smith P, Belting C, Castleman Z, Drake G, Espejo J, Heuerman K, Lanzi J and Stuchlik D. 2017. Radiometric flight results from the HyperSpectral Imager for Climate Science (HySICS). Geoscientific Instrumentation Methods and Data Systems, 6(1): 169-191. [DOI:10.5194/gi-6-169-2017]

Six Months of Preliminary Calibration Results of the Precipitation Measurement Radar onboard the FY-3G Satellite

By Honggang Yin (NSMC/CMA), Jian Shang (NSMC/CMA), Bosen Jiang (BRIT), Lei Cao (BRIT), Songyan Gu (NSMC/CMA), and Peng Zhang (NSMC/CMA)

As the first spaceborne precipitation mission in China, the FengYun-3G (FY-3G) satellite was launched on 16 April 2023. The nominal orbital altitude of the FY-3G satellite is 407 km, and the nominal orbital inclination is 50°. There are 4 operational payloads on the platform, including the Precipitation Measurement Radar (PMR), the passive microwave imager MWRI-RM, the optical medium resolution spectral imager MERSI-RM, and the global navigation satellite system occultation sounder GNOS-R. As the core instrument of the FY-3G satellite, the PMR is composed of a Ku-band radar and a Ka-band radar, and it adopts a planar slot waveguide

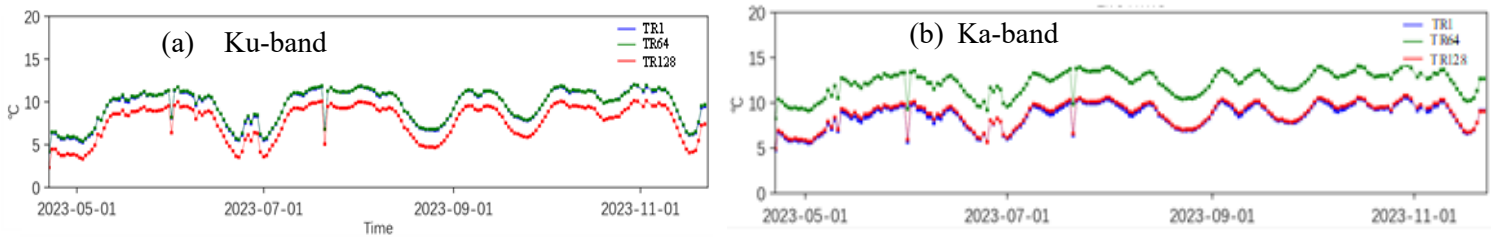

Figure 1. The PMR TR module's temperature variation

Return to Page One

doi: 10.25923/j6c7-9r34

array antenna to conduct electronic scanning in the cross-track direction of the orbit. The PMR uses variable pulse repetition frequency technology and four-frequency agility technology to achieve enough independent observing samples for all scanning angles. In the normal observation mode, the PMR can measure the rain echoes from -5 km under the sea level to 18 km height within the scanning angle range of ± 20.3°.

Compared to the Tropical Rainfall Measuring Mission (TRMM) Precipitation Radar (PR), the FY-3G PMR and the Global Precipitation Measurement mission (GPM) Dual-frequency Precipitation Radar (DPR) added the Ka-band radar, which can obtain more accurate precipitation measurements than single-frequency radar. Under the condition of equal horizontal resolution, the swath width of the PMR (300 km) is larger than both the TRMM PR and the GPM DPR. This helps the PMR to cover more precipitation events. In addition, the antenna peak sidelobe level of the PMR is lower than that of the TRMM PR and GPM DPR. This helps to suppress the influence of ground clutter and reduce measurement error.

The PMR started observation soon after its launch, and the data preprocessing segment began normal operation at the end of July. The instrument status is very stable ever since it was powered on, Figure 1 shows the temperature variation of the Transmitter/Receiver (TR) modules. At 22:19 (UTC) on May 25th, the FY-3G satellite flighted over Typhoon Mawa, the NASA GPM core satellite also flighted over the same location after 7 hours. Figure 2 compares their measured radar reflectivity factors

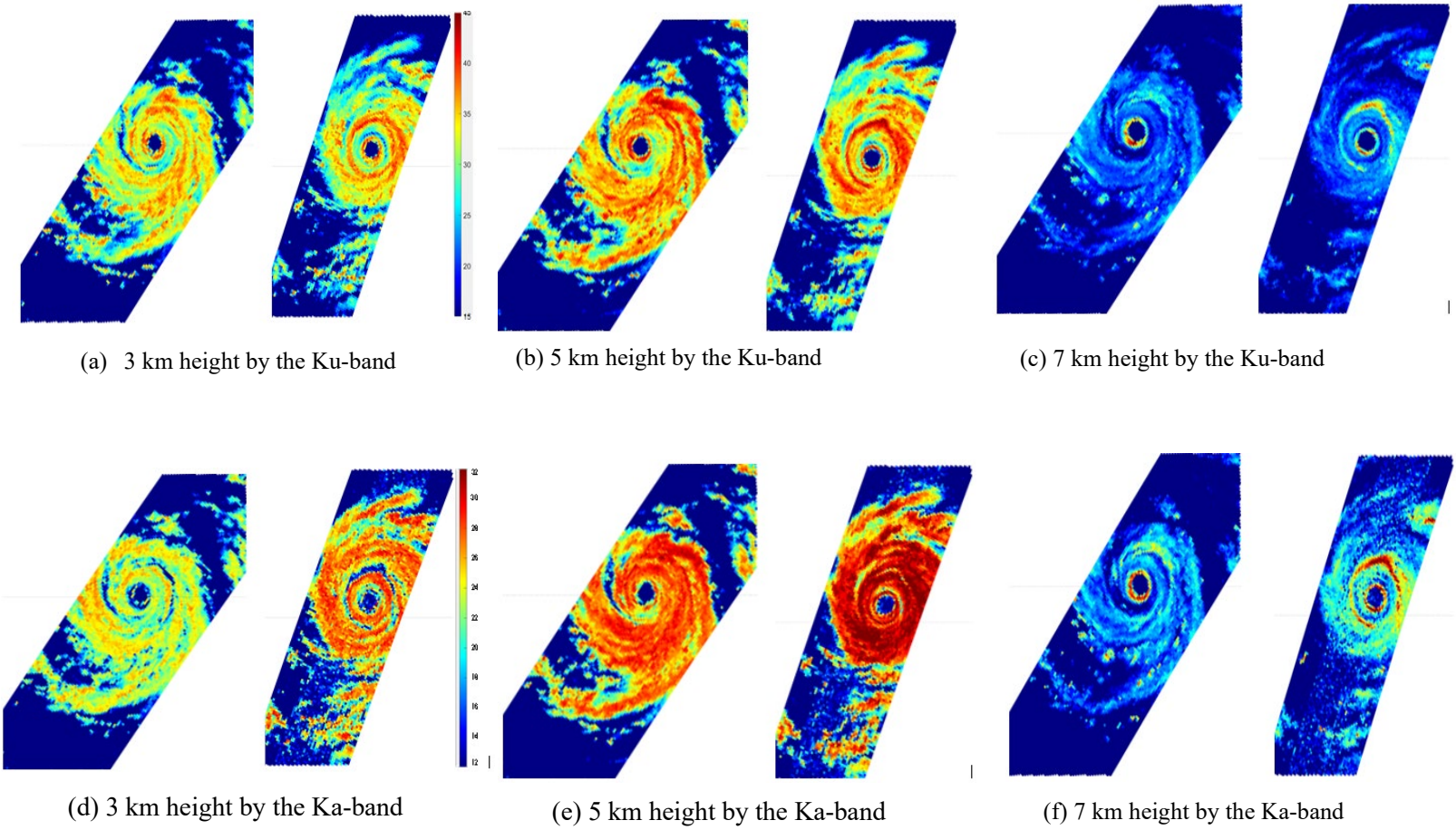

(a) 3 km height by the Ku-band (b) 5 km height by the Ku-band (c) 7 km height by the Ku-band

(d) 3 km height by the Ka-band (e) 5 km height by the Ka-band (f) 7 km height by the Ka-band

Figure 2. The measured radar reflectivity factors from PMR (left) and DPR (right) at different slanted heights from the earth surface along the radar boresight direction.

Return to Page One

doi: 10.25923/j6c7-9r34

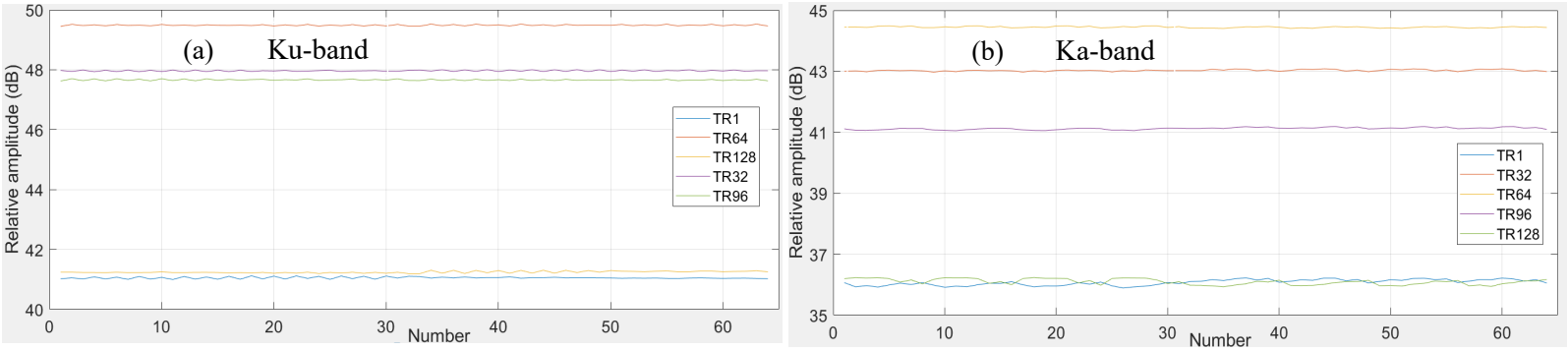

Figure 3. The relative amplitude of transmitted signal from different TR modules of the PMR achieved from the internal calibration on November 25th.

The accuracy requirement for the PMR precipitation measurement is 1dB, hence it is necessary to calibrate the PMR onboard. Calibration of the PMR consists of internal and external calibrations. The internal calibration is carried out once every day. During the internal calibration phase, the transmitted signal from each element of the waveguide slotted array antenna can be received by the couplers over the array plane, so the relative amplitude and phase between each TR module can be monitored. The relative amplitude of transmitted signals from different TR modules on November 25th is shown in Figure 3.

Since the internal calibration can't obtain information of the parameter changes of the whole radar, the external calibration is designed to absolutely calibrate the PMR. Figure 4 describes the schematic of the external calibration. A radar active calibrator (ARC) is deployed under the satellite track during the external calibration. The angle between the radar boresight and the line from the radar to the ARC is constantly changing during the satellite movement, so the radar antenna pattern can be measured. The ARC is able to operate in transmitting mode, receiving mode and transponding mode. Twenty-three external calibration experiments were conducted from August to September. These experiments showed that the PMR transmitting beamwidth and receiving beamwidth in both frequency bands on orbit changed by less than 3% compared to the ground test results. The maximum difference in transmitted/received beam direction between two bands is less than 0.02 degrees. Therefore, it can be concluded that the PMR has been working normally since its entry into orbit, and there is no need to revise its calibration parameters currently.

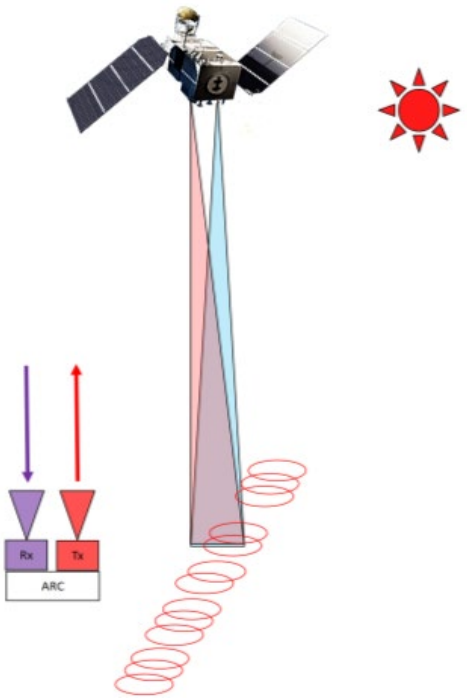

Figure 4. The schematic of the external calibration of the PMR using ARC

Return to Page One

doi: 10.25923/j6c7-9r34
GSICS Quarterly: Fall Issue 2023 Volume 17, No. 3, 2023

Cloud-Target Calibration for Fengyun-3D MERSI-II Solar Reflectance Bands: Model Development and Instrument Stability

By Chao Liu, Fukun Wang (Nanjing University of Information Science and Technology), Xiuqing Hu, and Peng Zhang (China Meteorological Administration)

Fengyun-3 (FY-3) is a series of Chinese flagship polar orbit meteorological satellites, and its fourth one, FY-3D has been operating since 2019. The second-generation Medium Resolution Spectral Imager (MERSI-II) onboard FY-3D is one of its most important instruments, and has 25 spectral bands centered between ~0.4 and 12 μm with spatial resolutions from 250 m to 1 km. MERSI-II is supposed to have absolute calibration accuracy of 5% in visible (VIS) and near-infrared (NIR) bands (Bands 1–19) and 0.5 K in infrared (IR) bands (Bands 20–25).

The MERSI calibration is mainly conducted using multiple global surface targets [2], which is the major operational method for Fengyun satellite radiometers. However, the calibrations that are based at the ground sites are often subject to disadvantages such as high maintenance costs, influences from weather conditions, and operation time limits. Thus, the MERSI-II calibration performance is less reported or known publicly after over five years, which substantially limits its applications. Meanwhile, abundant clouds in the atmosphere were potential targets for satellite calibration. Ham et al. [3] indicated that cloud targets are capable to be applied on monitoring the performance of Meteosat-8/9 and MTSAT-1R, whereas their method is limited to cloud non-absorbing bands, and such a cloud-based calibration has been less reported or used since then.

Alleviating the aforementioned difficulties in providing an accurate and timely calibration for the MERSI-II bands, we developed an all-cloud target (ACT) calibration method for six MERSI-II reflective solar bands (RSBs), including three VIS bands (Bands 1–3, centered at 0.46, 0.55, and 0.65 μm, respectively) and three NIR bands (Band 4 centered at 0.87 μm and Bands 6 and 7, centered at 1.61 and 2.13 μm, respectively) [4], and reported and corrected the current MERSI-II reflectance biases to improve its calibration accuracy.

For our ACT calibration, collocated Moderate Resolution Imaging Spectroradiometer (MODIS) cloud products, mainly the cloud optical thickness (COT) and cloud effective radius (CER), are used to provide reliable cloud information, and a rigorous discrete ordinates radiative transfer (DISORT) model is used to simulate the top-of-atmosphere (TOA) reflectance of both MODIS (for model validation) and MERSI-II (for calibration). To limit possible errors due to collocation or parallax, restrictive conditions are applied in the selection of cloud targets:

1. Only non-sunglint pixels located between 30°N~30°S are considered.
2. Both optically thin clouds with a COT < 10 and optically thick clouds with a COT > 150 are eliminated to avoid uncertainties introduced by the MODIS cloud property retrievals.
3. Cloudy targets must also satisfy three homogeneity checks, i.e., the ratios of the standard deviation of the 9 × 9 surrounding pixels and their average values for the 0.65-μm reflectance, COT, and CER must be less than 0.03, 0.1, and 0.03, respectively.

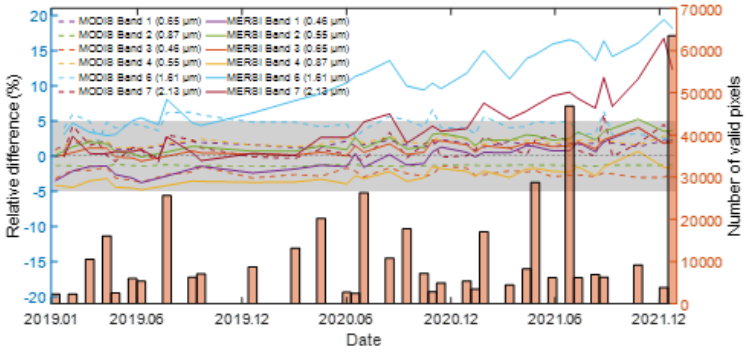

Fig. 1. Time series of RDs between the current MODIS (dashed) and MERSI-II (solid) calibrated reflectance and our simulations over three years (2019–2021), and the number of valid collocated MODIS and MERSI-II cloudy pixels.

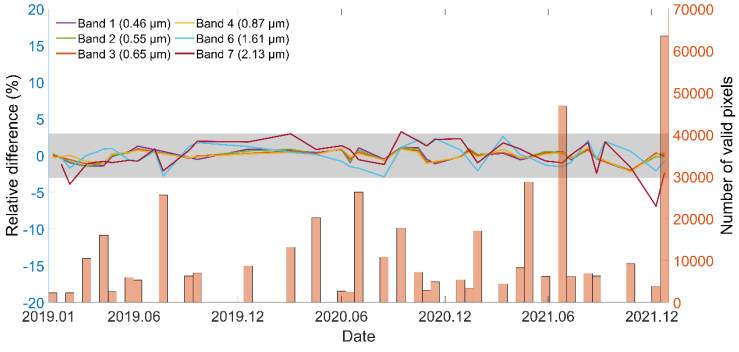

Fig. 2. Time series of RDs between the MERSI-II reflectance after correcting the degradation and our simulations over three years (2019–2021); the gray region indicates the 3% uncertainty range.

doi: 10.25923/j6c7-9r34

Thus, a direct comparison between our simulated reflectance and MERSI-II operational Level-1 reflectance for the cloudy targets can be understood to infer their current calibration performance, and such comparisons for MODIS are also performed for model validation. Time series of the average relative differences (RDs) between the simulated and current calibrated reflectance for the 2019–2021 period are shown in Fig. 1. The RDs are calculated and averaged only if there are over 2000 qualified pixels within the sample bin (a 15-day period), and there are 35 validated samples during the 2019–2021 period (the maximum possible number is ~73, i.e., ~50%). The time series for MODIS results show relatively stable variations for all six bands (although there may be systematic REs reaching almost 5%). REs for four MERSI-II bands (Bands 1–4) are also relatively stable, while the two NIR bands (Bands 6 and 7) show obviously increasing trends on their RDs. The RDs of Band 6 have the largest changes, increasing almost 20% within the three years. Generally, there are increasing trends for the six MERSI-II bands to different degrees, which are thought to be associated with sensor degradation during the three-year period, because the current MERSI-II operational calibration uses consistent calibration coefficients.

Since the time series shown in Fig. 1 suggests annual biases in the current MERSI-II operational measurements, it may be possible to remove these biases to get better-calibrated reflectance. We consider such systematic RD variations to be sensor degradations of each band, and intend to remove them by using a linear equation as follows:

$$RD = A \times T + B \quad (1)$$

Here, A and B represent coefficients considered to fit the MERSI-II RD time series in Fig. 1. T represents the time variable in the form of normalized Julian day, so that coefficient A can represent the sensor degradation rate (in a unit of percentage per year), and larger A values indicate larger degradation. RD is the relative differences between our simulated and operational calibrated reflectance for each band, expressed in a unit of percentage (%). Table 1 lists fitted values of the two coefficients for each MERSI-II band. Notice that coefficient A is associated with the time, so it is in a unit of degradation rate/year. The adjusted R-square (R^2_{ad}) and root-mean-square deviation (RMSE) are used to indicate the performance of the fitting. The degradation is relatively small in Bands 2–4 with rates of approximate or less than ~1% per year. A relatively larger degradation rate is found in Band 1, whose coefficient A reaches 1.85% per year. The two-cloud absorbing NIR bands exhibit much larger degradation, with annual degradation rates of 5.05% and 3.86% for Bands 6 and 7, respectively.

Band	A	B	R^2_{ad}	RMSE
Band 1 (0.46 μm)	1.85	−3.29	0.80	0.85
Band 2 (0.55 μm)	1.04	0.36	0.59	0.76
Band 3 (0.65 μm)	0.76	−0.12	0.49	0.69
Band 4 (0.87 μm)	1.06	−4.52	0.67	0.68
Band 6 (1.61 μm)	5.05	2.49	0.91	1.47
Band 7 (2.13 μm)	3.86	−1.48	0.76	2.03

Table 1: Coefficient values for the six MERSI-II bands and the adjusted

With the fitted coefficients, it becomes straightforward to correct the current MERSI-II operational reflectance for the six RSBs, and the RDs after the degradation errors corrected are shown in Fig. 2. Specifically, the RDs in Fig. 2 are obtained by subtracting the corresponding errors from the fitted lines from the original ones in Fig. 1. With the degradation errors corrected, most RDs become within the ±3% range, which is marked by the gray area. There is only one outlier with a RD of approximately 5% for Band 7, which could be attributed to the simulation uncertainty for cloud-absorbing bands or a relatively limited number of valid pixels in the corresponding period. Compared to Fig. 1, our ACT method and the correction clearly improve the stability of current MERSI-II RSB calibration, making it within a 3% uncertainty range (better than the officially reported calibration accuracy of 5%).

To summary, Wang et al. [4] developed an ACT-based calibration method and examined the operational performance of six MERSI-II RSBs of the Chinese FY-3D. In the work, measured reflectance and cloud products obtained by MODIS were used as a reference, because MODIS carries a set of on-orbit calibration systems and can ensure high accuracy (3%). The ACT-based method used collocated COT, CER, and cloud phases obtained from the MODIS cloud product for radiative transfer to simulate the TOA reflectance of the six cloud-sensitive RSBs. To minimize the influences due to collocation and cloud target properties, strict thresholds are applied to the cloudy target selection.

Return to Page One

doi: 10.25923/j6c7-9r34

The RDs of the long-term (three years)simulation results are within 3% for MERSI-II Bands 1–4, while the results of MERSI-II Bands 6 and 7 show relatively larger RDs and increasing trends due to the significant sensor degradation. By fitting the RDs with linear functions, the signal degradations were quantified and removed. Band 1 shows the degradation rate of 1.85% per year. For the two cloud-absorbing bands, sensor degradation becomes more significant, reaching 5.05% (Band 6) and 3.86% (Band 7) per year, respectively. After the correction with the fitted functions, most of the differences between the simulation and the corrected reflectance are improved to be within the 3% uncertainty range, and no obvious temporal trend was noticed. These results demonstrated that the ACT-based calibration method is reliable for the six MERSI-II RSBs and has the potential to be further applied in calibration work for the MERSI-II and other Fengyun instruments.

References

[1]. L. Zhou, M. Divakarla, and X. Liu, "An overview of the Joint Polar Satellite System (JPSS) science data product calibration and validation," Remote Sens., vol. 8, no. 2, pp. 139, Feb. 2016, doi: 10.3390/rs8020139.

[2]. L. Wang, X.-Q. Hu, and L. Chen, "Wide dynamic nonlinear radiometric calibration of optical satellite sensors using multiple stable earth targets," J. Remote Sens., vol. 21, no. 6, pp. 892–906, 2017, doi: 10.11834/jrs.20176351.

[3]. S.-H. Ham and B. J. Sohn, "Assessment of the calibration performance of satellite visible channels using cloud targets: Application to Meteosat-8/9 and MTSAT-1R," Atmos. Chem. Phys., vol. 10, no. 22, pp. 11131–11149, Nov. 2010, doi: 10.5194/acp-10-11131-2010

[4]. F. Wang, C. Liu, B. Yao, X. Hu, P. Zhang, and B. J. Sohn. "Cloud-target calibration for Fengyun-3D MERSI-II solar reflectance bands: model development and instrument stability," *IEEE Trans. Geosci. Remote Sens.*, vol. 61, no. 5401313, pp. 1-13, Feb 2023, doi: 10.1109/TGRS.2023.3244949.

NEWS IN THIS QUARTER

3rd FengYun Satellite User Conference (FY-2023) held from 13-14 November 2023 in Xiamen, China

By Pengjuan Yao, Fangli Dou, Jian Shang, Ling Sun, Chengli Qi, Shengli Wu, Xiuqing Hu, Na Xu, Di Xian, and Peng Zhang (NSMC/CMA)

The 3rd FengYun Satellite User Conference (FY 2023) was held in Xiamen, Fujian province, China November 13-14, 2023. The conference was hosted by China Meteorological Administration (CMA) and China National Space Administration (CNSA), organized by National Satellite Meteorological Center/National Center for Space Weather (CMA/NSMC) and Shanghai Academy of Spaceflight Technology (SAST), co-organized by Fujian Provincial Meteorological Service, National Meteorological Center, China Meteorological Administration Training Center, Innovation Center for FengYun Meteorological Satellite and Beijing Huayun Shinetek Science and Technology Co. Ltd. Over 200 participants from 25 countries attended the conference.

Photo: Participants of the FY 2023 at Xiamen, China

Return to Page One

doi: 10.25923/j6c7-9r34

Opening remarks

In the opening ceremony, Member of the Fujian Leading Party Members Group, Kang Tao, welcomed all participants from 25 countries. The President of WMO, Abdulla Al Mandous, delivered an opening remark via video. He thanked China for the important role of Chinese satellite program in WMO integrated global observation system (WIGOS) vision and the international CHARTER on space and major disaster. He urged all the participants to actively engage in the conference.

The Chief Engineer of CNSA, Guoping Li, delivered a speech representative of CNSA. He mentioned the rapid development of China's aerospace enterprise, and the close collaboration with CMA, especially in constructing a complete meteorological satellite system. He stressed CNSA will further improve its civilian space infrastructure to better meet the global users' requirements and promote spatial information to serve long-term sustainable economic and social development.

The Administrator of CMA, Zhenlin Chen, presented a summary of the service of FengYun Satellite to the international community. He mentioned that FengYun constellation had served 129 countries and regions. Particularly for along the 'Belt and Road' initiative, FengYun satellites have provided emergency disaster mitigation services about 140 times via the Emergency Support Mechanism of FengYun Satellite (FY_ESM). More than 11000 international students have received CMA training in data usage and software application. Dr. Chen highlighted the willingness to actively expand cooperation with international organizations and countries, and to jointly promote the development of global meteorological undertakings.

Launch announcement.

FengYun-3F First Images

The Director-General of the CMA Department of Integrated Observations, Xiang Fang, announced the release of the first images captured by FengYun-3F (FY-3F). The first images show FY-3F's capabilities in imaging, sounding, observing radiometric budget of the Earth-atmosphere system and atmospheric composition. The FY-3F satellite was successfully launched on August 3rd, 2023, as the "successor" to FengYun-3C. It carries ten remote sensing instruments, of which two are newly developed UV hyperspectral instruments. All ten remote sensors onboard FY-3F have been turned on and are in commissioning phase. FY-3F is expected to enter the trial operational phase in March 2024, and will be officially operational to provide global data services during the flood-prone season next year.

FengYun-3G Global Data

FengYun-3G (FY-3G), the first precipitation measurement satellite of China, was successfully launched on April 16th this year. It operates stably in orbit with all instruments in good condition. Recently, the first commissioning phase has been completed. The FY-3G level-1 data are officially released to the world and can be accessed through the FengYun Satellite Remote Sensing Data Service network. (Website link: http://data.nsmc.org.cn/PortalSite/Default.aspx)

International FengYun Satellite Application Competition

The Director-General of the CMA Department of International Cooperation, Qian Zeng, launched the FengYun Satellite International Application Competition at this conference. This competition focuses on meteorological satellite applications and new digital technologies, such as big data and artificial intelligence (AI). It aims to promote the application of satellite remote sensing data and encourages international users to provide feedback on the achievements of FengYun satellite applications. (Website link: www.nsmc.org.cn/conference/CONTEST/cn/index.html)

The 'Belt and Road' Meteorological Visiting Scholar Program

The Director-General of the CMA Department of Human Resources, Zhihua Wang, announced the initial cohort for the 'Belt and Road' Meteorological Visiting Scholar Program. This program was jointly established by CMA and the Ministry of Education (MOE) under the framework of the 'Silk Road' Chinese Government Scholarship in September 2023. They announced the recruitment of outstanding talents from the meteorological and hydrological government departments of Belt and Road countries. Eight experts from Pakistan, Thailand, Ethiopia and Tanzania will come to China as the first batch of visiting scholars for further study. The Program is a long-term cooperation project between CMA and MOE. It encourages talents from Belt and Road countries to come to China and contribute to the technological innovation of FengYun satellites.

The FengYun Earth

The Director-General of NSMC/CMA, Jinsong Wang, announced the official release of *FengYun Earth* application. Based on the existing FengYun Earth platform, which has been extensively

Return to Page One

doi: 10.25923/j6c7-9r34

utilized in China's meteorological system, this version was developed in response to the demand of diverse international users. *FengYun Earth* offers **real-time, smart, refined, and customizable** satellite remote sensing application services to users worldwide. Users can receive satellite images in a short span of just six minutes. The platform enables the intelligent identification of extreme weather and climate events and offers over 100 quantitative products across five categories. It also boasts robust customization features catering to the specific needs of different countries and regions. (Website link: http://fyearth.nsmc.org.cn/)

Announcements

GSICS Annual Meetings in Darmstadt, Germany, 11-15 March 2024

By Tim Hewison (EUMETSAT)

EUMETSAT will host the 2024 annual meeting of the GSICS Research and Data Working Groups in Darmstadt, Germany. The meeting will cover the full working week from 11 to 15 March. It will include sessions for the four spectral sub-groups (Vis/NIR, UV/Vis/NIR Spectrometer, Infrared and Microwave), as well as the new Space Weather sub-group. For the first time, it will incorporate a meeting of the GSICS Executive Panel on 14 to 15 March, which aims to increase integration, while reducing travel overheads. Remote attendance will also be possible. Invitations will be sent to official representatives and registration will open early January 2024. More details will be available on the GSICS Development Wiki.

SPIE Optics and Photonics Earth Observing Systems Conference to be held in San Diego Aug 18-22, 2024

By Xiaoxiong (Jack) Xiong (NASA GSFC), Xingfa Gu (CAS), and Jeffrey S. Czapla-Myers (University of Arizona)

The annual SPIE Optics and Photonics' Earth Observing Systems XXIX Conference will be held August 18-22, 2024, at the San Diego Convention Center, San Diego, CA.

The Earth Observing Systems XXIX, Conference welcomes the submission of papers over a wide range of remote sensing topics. Papers are being solicited in the following general areas:

- Earth-observing mission studies including new system requirements and plans
- commercial system designs
- electro-optical sensor designs and sensitivity studies
- ultraviolet through thermal infrared, microwave, radar, and lidar remote sensing systems
- hyperspectral remote sensing instruments and methodologies
- instrument sub-system and system level pre-launch and on-orbit calibration and characterization
- vicarious calibration techniques and results
- satellite instrument airborne simulators
- techniques for enhancing data processing, reprocessing, archival, dissemination, and utilization
- conversion from research to operational systems
- on-orbit instrument inter-comparison techniques and results
- enabling technologies (optics, antennas, electronics, calibration techniques, detectors, and models)
- sensor calibration traceability, uncertainty, and pre-launch to on-orbit performance assessments
- lunar radiometry and photometry
- remote sensing data acquisition and analysis.

Return to Page One

GSICS Related Publications

Daniel Saul Goldin, Rajendra Bhatt, and Yolanda Shea. 2023. 'Evaluation of Systematic Errors on Polarization Parameters from POLDER Instrument Data for Use in CLARREO Pathfinder-VIIRS Intercalibration'. *Journal of Applied Remote Sensing* 17 (3): 034513. https://doi.org/10.1117/1.JRS.17.034513.

Loveless, M, R Knuteson, H Revercomb, L Borg, D DeSlover, G Martin, J Taylor, F Iturbide-Sanchez, and D Tobin. 2023. 'Comparison of the AIRS, IASI, and CrIS Infrared Sounders Using Simultaneous Nadir Overpasses: Novel Methods Applied to Data From 1 October 2019 to 1 October 2020'. *EARTH AND SPACE SCIENCE* 10 (7). https://doi.org/10.1029/2023EA002878.

Lyapustin, A, YJ Wang, M Choi, XX Xiong, A Angal, AS Wu, DR Doelling, et al. 2023. 'Calibration of the SNPP and NOAA 20 VIIRS Sensors for Continuity of the MODIS Climate Data Records'. *REMOTE SENSING OF ENVIRONMENT* 295 (September). https://doi.org/10.1016/j.rse.2023.113717.

S. Liu, B. Wu, C. -Z. Zou, and Y. Wang. 2023. 'Highly Consistent Brightness Temperature Fundamental Climate Data Record from SSM/I and SSMIS'. *IEEE Transactions on Geoscience and Remote Sensing*, 1–1. https://doi.org/10.1109/TGRS.2023.3316694

Submitting Articles to the GSICS Quarterly Newsletter:

The GSICS Quarterly Press Crew is looking for short articles (800 to 900 words with one or two key, simple illustrations), especially related to calibration / validation capabilities and how they have been used to positively impact weather and climate products. Unsolicited articles may be submitted for consideration anytime, and if accepted, will be published in the next available newsletter issue after approval / editing. Please send articles to manik.bali@noaa.gov.

With Help from our friends:

The GSICS Quarterly Editor would like to thank the Guest Editor of the Special Issue: Peng Zhang (CMA).
A special thanks for our expert reviewers, Dave R. Doelling (NASA), Larry Flynn (NOAA),Tim Hewison(EUMETSAT), Sri Harsha Madhavan (SSAI), Cheng-Zi Zou (NOAA) and Manik Bali (UMD) for reviewing articles in this issue. Special thanks to Chengli Qi (CMA) for facilitating the special issue. Thanks to Jan Thomas (NOAA) for ensuring 508 compliance of the issue.

Published By

GSICS Coordination Center
NOAA/NESDIS/STAR NOAA
Center for Weather and Climate Prediction, C
5830 University Research Court, C2850
College Park, MD 20740, USA

Return to Page One